

RESEARCH ARTICLE

10.1002/2015JD024186

This article is a companion to Heiblum et al. [2016] doi:10.1002/2015JD024193.

Key Points:

- Introducing 3-D cloud tracking and cloud center of gravity versus mass (CvM) phase space
- Trajectories in the CvM space reveal cloud field characteristics
- Cloud clustering in the CvM space shows the role of the thermodynamic profiles

Correspondence to:

I. Koren,
ilan.koren@weizmann.ac.il

Citation:

Heiblum, R. H., et al. (2016), Characterization of cumulus cloud fields using trajectories in the center of gravity versus water mass phase space: 1. Cloud tracking and phase space description, *J. Geophys. Res. Atmos.*, 121, 6336–6355, doi:10.1002/2015JD024186.

Received 4 SEP 2015

Accepted 7 APR 2016

Accepted article online 5 MAY 2016

Published online 7 JUN 2016

Characterization of cumulus cloud fields using trajectories in the center of gravity versus water mass phase space:

1. Cloud tracking and phase space description

Reuven H. Heiblum¹, Orit Altaratz¹, Ilan Koren¹, Graham Feingold², Alexander B. Kostinski³, Alexander P. Khain⁴, Mikhail Ovchinnikov⁵, Erick Fredj¹, Guy Dagan¹, Lital Pinto¹, Ricki Yaish¹, and Qian Chen¹
¹Department of Earth and Planetary Sciences, Weizmann Institute of Science, Rehovot, Israel, ²Chemical Sciences Division, NOAA Earth System Research Laboratory, Boulder, Colorado, USA, ³Department of Physics, Michigan Technological University, Houghton, Michigan, USA, ⁴The Institute of Earth Sciences, Hebrew University of Jerusalem, Jerusalem, Israel, ⁵Atmosphere Science and Global Change Division, Pacific Northwest National Laboratory, Richland, Washington, USA

Abstract We study the evolution of warm convective cloud fields using large eddy simulations of continental and trade cumulus. Individual clouds are tracked a posteriori from formation to dissipation using a 3-D cloud-tracking algorithm, and results are presented in the phase space of center of gravity altitude versus cloud liquid water mass (CvM space). The CvM space is shown to contain rich information on cloud field characteristics, cloud morphology, and common cloud development pathways, together facilitating a comprehensive understanding of the cloud field. In this part we show how the meteorological (thermodynamic) conditions that determine the cloud properties are projected on the CvM phase space and how changes in the initial conditions affect the clouds' trajectories in this space. This part sets the stage for a detailed microphysical analysis that will be shown in part II.

1. Introduction

Clouds and precipitation play crucial roles in the climate system as they influence the Earth's energy and water budgets [Baker and Peter, 2008; Trenberth et al., 2009]. A cloud field is a complex product of processes at various scales. At the macroscale environmental conditions (temperature, humidity, and wind profiles) determine the thermodynamic potential for cloud development, and at the microscale aerosols serve as cloud condensation nuclei (CCN) required for the formation of the cloud droplets at the available supersaturation. In this study we focus on warm (liquid only) convective cloud fields that are less complex than mixed-phase clouds but are still not well understood. Warm cumulus clouds cover vast areas of the ocean (12%) and land (5%) [Warren et al., 1986; Warren et al., 1988]. They play a major role in the transport of moisture, heat, and aerosol to the free atmosphere. Changes in these clouds resulting from changes in aerosol properties or meteorological settings can impact the energy budget [Bony and Dufresne, 2005; Wielicki et al., 2005] and the hydrological cycle [Short and Nakamura, 2000].

Separation of meteorological (thermodynamic) and aerosol effects is difficult because the microphysical processes are tightly coupled to cloud dynamics via their influence on latent heating, drag forces, droplet terminal velocities, evaporation rates, and supersaturation relaxation. The atmosphere constantly readjusts as the cloud field evolves, which may result in both weaker or magnified responses [e.g., Stevens and Feingold, 2009]. To try to separate individual processes in a coupled system, a cloud-resolving model or large eddy simulation (LES) can be used. Using such models, simulations can be performed for the same meteorological conditions changing only the aerosol properties [Khain, 2009; Tao et al., 2012]. Similarly, one can fix the aerosol concentration and force changes in the meteorological conditions. Assuming that the prescribed physics is accurate enough for the question at hand, the use of numerical models allows one to check the system sensitivity to changes in given parameters. However, generalization of the results and capturing the contribution of the coupled terms is challenging.

In this paper we will analyze output from LES of warm convective cloud fields. In addition to domain-wide cloud field properties, we also track individual clouds through their lifetime. Results are presented in a thermodynamic space defined as center-of-gravity altitude (COG) versus water mass (cloud mean

liquid water path (LWP) or cloud total mass), hereafter CvM space, where the center of gravity altitude is the average height of the cloud weighted by the mass, defined as [Grabowski *et al.*, 2006; Koren *et al.*, 2009]:

$$\text{COG} = \frac{\sum_i m_i z_i}{M} \quad (1)$$

where m_i and z_i are the respective mass [kg] and height [m] of voxel i of a cloud, and M the total water mass of the cloud. This representation in the CvM space bears similarity to graphs of observed profiles of liquid water content as a function of height in clouds [Cotton *et al.*, 2011], but its advantage is that it reduces the dimensionality of the problem and represents the whole cloud field with many of its inherent complexities in a single phase space that reflects both thermodynamic and microphysical properties. We demonstrate how trajectories in the proposed phase space describe common pathways of warm cumulus clouds under different environmental and microphysical conditions, and their evolution in time.

2. Model Description and Setup

We use the System for Atmospheric Modeling (SAM) model (version 6.10.3) for conducting LES simulations [Khairoutdinov and Randall, 2003] (for details, see webpage: <http://rossby.msrc.sunysb.edu/~marat/SAM.html>). SAM is a nonhydrostatic, anelastic model. Cyclic horizontal boundary conditions were used together with damping of gravity waves and maintaining temperature and moisture gradients at the model top. An explicit Spectral Bin Microphysics scheme [Khain *et al.*, 2004] is used, which has been recently implemented in SAM and tested in several studies [Fan *et al.*, 2009; Khain *et al.*, 2013]. The scheme solves all warm microphysical processes, including droplet nucleation, diffusional growth, collision coalescence, sedimentation, and breakup. The model is initialized using an oceanic size distribution of ammonium-sulfate aerosols [Jaenicke, 1988; Altaratz *et al.*, 2008], maintaining constant mixing ratio with height. The aerosol size distribution is truncated between 5 nm and 2 μm (smallest and largest aerosol bin radius size). The aerosols serve as potential cloud condensation nuclei (CCN) and undergo activation based on Kohler theory [Khain *et al.*, 2000]. We solve a prognostic equation for the aerosol, which includes regeneration upon evaporation and removal by surface rain. The aerosol concentration can be depleted by 20%–40% (depending on the precipitation amount) during an 8 h simulation. The water drop bin radii range between 2 μm and 3.2 mm. For diagnostic purposes, a threshold of 40 μm radius is used to separate cloud droplets and rain drops. For both aerosol and water species, successive bins represent doubling of mass.

Two different cases are simulated. 1. The Barbados Oceanographic and Meteorological Experiment (BOMEX) [Holland and Rasmusson, 1973; Siebesma *et al.*, 2003] case study (named BOMEX-orig) that simulates a trade wind cumulus cloud field based on observations made near Barbados during June 1969. This case is initialized using the setup specified by the GEWEX Cloud System Study Boundary Layer Cloud Working Group. 2. An Amazon cumulus case based on the afternoon dry season mean profile for August 2001 that was obtained during the Large-scale Biosphere-Atmosphere experiment data at Belterra, Brazil [Dias *et al.*, 2012].

To test meteorological effects on cloud evolution in the CvM space, low inversion (BOMEX-lowinv) and high inversion (BOMEX-highinv) versions of the BOMEX profile are simulated as well for a total of three BOMEX simulations (Figure A1). The low (high) inversion soundings are created by lowering (raising) the inversion layer height in the original profile by 500 m, while keeping both temperature and moisture gradients constant in the subcloud, cloud, and inversion layers. All four soundings (three BOMEX and one Amazonian) and surface properties used to initialize the model are presented in Figure A1 and Table A1. Comparison of aerosol effects on BOMEX cloud fields is the topic of Part II of this work.

The grid size is set to 100 m in the horizontal direction and 40 m in the vertical direction for all simulations. The domain size is 12.8 km \times 12.8 km \times 4 km for the BOMEX simulations and extended to 6 km in the vertical direction for the Amazon run. The time step for computation is 1 s for all simulations, with a total runtime of 8 h. The initial temperature perturbations (randomly chosen within $\pm (0.1\text{--}1)^\circ\text{C}$) are applied near the surface, during the first time step.

3. Cloud Tracking

The purpose of a cloud-tracking algorithm is to track the evolution of a predefined set of properties defining an individual cloud through its life cycle. Previous cloud-tracking algorithms have been developed for models based on 2-D projections of the cloud [Jiang et al., 2006; Heus and Seifert, 2013], 3-D volumes [Zhao and Austin, 2005; Heus et al., 2009; Plant, 2009; Dawe and Austin, 2012], and for radar data [Handwerker, 2002]. In addition to the general requirement to analyze the average properties of a cloud field such as cloud fraction or mean LWP, there is added value in following individual cloud evolution in order to enable investigation of different stages of cloud lifetime and the interactions between clouds. Using a newly developed 3-D cloud-tracking algorithm (see detailed description below), we collected more than 40 different parameters that describe various cloud characteristics, including cloud water mass, rain water mass, cloud base and top height, horizontal cross-section area, shaded area, COG of total liquid water (and of cloud droplets and raindrops), updraft speeds, liquid water content (LWC), and buoyancy profiles (see Table B1 for the complete list). The advantages of this 3-D algorithm include its automatic ability to track a large number of relatively small clouds, to recognize splitting and merging events, and to keep record of the parent clouds (e.g., which cloud was the original cloud that split into two new clouds). All of the above make it a very useful tool for tracking cumulus cloud properties for investigation of their associated physical processes in time.

3.1. Method Description

The 3-D cloud-tracking algorithm is based on post simulation processing of 1 min interval output files from the LES model and is composed of four main stages: (1) cloud formation identification at a specific time (proto clouds), (2) tracking the clouds over the course of their lifetime, (3) identification of merge and split events, and (4) determination of “Continuous Cloud Entities” (hereafter CCE)—clouds that start as proto clouds and keep their identity through insignificant merge and split events. The details of each step are as follows:

1. *Cloud identification.* The cloudy voxels are determined as voxels with liquid water content (either cloud, rain, or both) above a threshold of 0.005 g kg^{-1} [Cohen and Craig, 2006]. Adjacent cloudy voxels are labeled as one cloud by a 3-D 26 segment method (allowing for connections along a diagonal). We apply a minimal threshold of four adjacent voxels to label a cloud; the smaller cloudy objects are ignored.
2. *Tracking a cloud over the course of its lifetime.* Each labeled cloud is tracked for subsequent analysis. The link between successive locations of a specific cloud is done by assuming its next position (in the next output) based on the local advection field. The first approximation of a cloud location “guess” is done by advancing the cloudy voxels according to the corresponding wind vectors. This guess of cloud position and shape is then compared to the simulated clouds in the next time step. If there is an overlap in the cloudy voxel positions between the guess and a simulated cloud, then it is determined to be the same cloud. In a horizontally periodic domain the tracking algorithm follows clouds as they move from one boundary through the opposite one and back into the domain.
3. *Identification of proto, merged, and split clouds.* Simulated clouds that do not overlap with any cloud guess from the previous time step are given a new label and classified as *proto* clouds (i.e., proto clouds are new clouds). When a previous time step cloud guess overlaps with only one simulated cloud, it is determined to be the same cloud and retains its label and classification type (i.e., proto, split, or merged). In the case that the overlap is with more than one simulated cloud, the simulated clouds are classified as *split* clouds and acquire new labels, as we assume that the “parent” cloud has split into two or more “children.” In the case that the guesses of two or more clouds overlap with one simulated cloud, the cloud is classified as a *merged* cloud and acquires a new label (i.e., the old clouds’ lifetimes are terminated as a new merged cloud is just born). For all cloud cases, information about their parent or children clouds is also saved in the cloud-tracking data set in order to enable the tracking of the full history of every cloud.
4. *Determination of Continuous Cloud Entities (CCE).* As a last step in the tracking algorithm we use all the collected data (for the categories proto, merged, and split clouds) for selecting and following the evolution of CCE clouds. This new category represents clouds that keep their identity through insignificant merge and split events. These clouds begin as proto clouds but can then merge with other clouds or split under the condition that they comprise at least 75% of the splitting/merging total water mass summation (e.g., if a proto cloud splits into two clouds of 200 kg and 1000 kg each, the 1000 kg cloud represents 83% of their sum and thus that cloud continues to be a CCE).

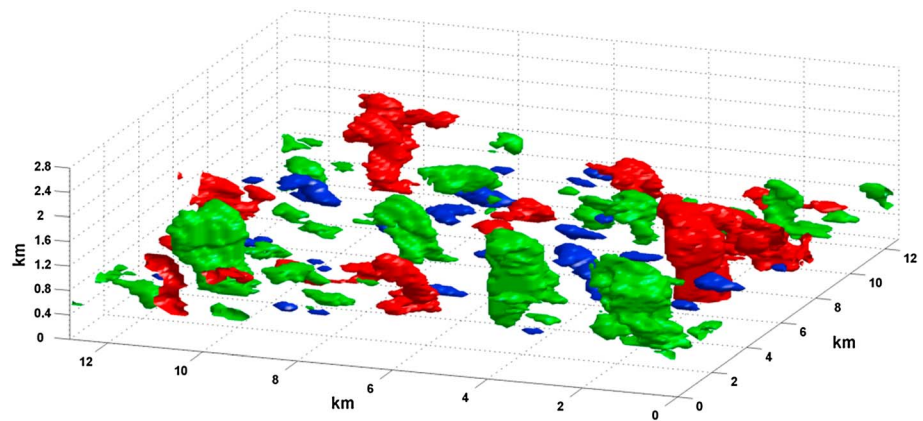


Figure 1. Three-dimensional snapshot of BOMEX 500 cm^{-3} domain after 3.5 h of simulation. Proto clouds are represented by blue colors, split clouds by green colors, and merged clouds by red colors.

4. Results and Discussion

4.1. Cloud-Tracking Algorithm Results

The results of the tracking algorithm are demonstrated here for the BOMEX-orig case with an aerosol concentration of 500 cm^{-3} . The total time of the simulation is 8 h, and cloud-tracking statistics are analyzed from 3 h (allowing sufficient spin-up time) to 7 h of simulation time in order to avoid cases of incomplete tracking of the entire cloud lifetime. A total of 4543 clouds are tracked (not including different time steps of the same cloud), of which 26.7%, 58.5%, 14.8% are categorized as proto, split, and merge types, respectively. Since CCE clouds are all initiated from proto clouds, their numbers are identical.

In Figure 1 a 3-D snapshot of the cloud field after 3.5 h of simulation is shown. The blue, green, and red colored clouds correspond to proto, split, and merged type clouds, respectively. Visual tracking of the 3-D field cloud type evolution serves as a simple sanity check for the cloud-tracking algorithm output. As can be expected, the small and medium sized clouds with low-altitude base are typically proto or split clouds, and the large, more developed clouds tend to be either split or merged. Generally, clouds that live more than a few minutes tend to undergo a split event, thus yielding a majority of split type clouds in the domain.

Figure 2 presents the histograms of lifetime, maximum total water mass, and maximum equivalent radius (i.e., circular radius which corresponds to the observed cloud maximum cross-sectional area) of five different

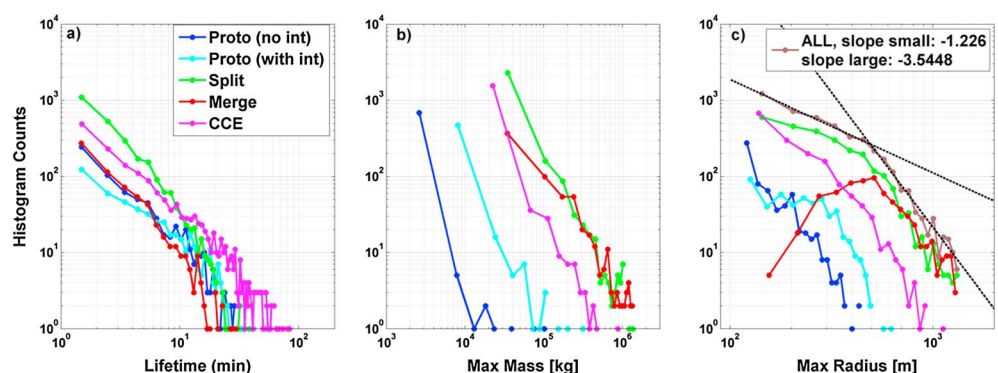


Figure 2. Log-log histograms of the BOMEX 500 cm^{-3} simulation cloud characteristics. (a) Cloud lifetime, (b) maximum cloud mass during lifetime, and (c) maximum cloud radius during lifetime. Radii values start from $\sim 116 \text{ m}$ (equivalent radius of four horizontal voxels minimum cloud threshold) since clouds with smaller radii were rare and excluded here. Each panel shows proto clouds that did not interact along their whole lifetime (blue curve), proto clouds until they went through a merge or split event (cyan curve), split clouds (green curve), merge clouds (red curve), and CCE (magenta curve). The maximum radius histogram also includes a combined histogram of all cloud types (brown curve), with power law fit exponent values in the panel legend.

subsets of clouds during their lifetimes. The subsets are of proto clouds that remained proto throughout their lifetime (marked as “no int” in Figure 2), proto clouds until the point they either merged or split (“with int” in Figure 2), split clouds, merged clouds, and CCEs. For proto, merge, and split types, cloud lifetime represents the time span between being classified and either changing classification or dissipating (e.g., in the case a proto cloud lives for 1 min, and then splits to two clouds that live for 1 min each and dissipate, the lifetimes of all three will be 1 min). For CCEs, lifetime may represent a complete life cycle of a cloud, from initial formation (proto) to dissipation. The lifetime of the clouds in all the categories, except the CCEs, is between a few minutes to 30 min for a few “lucky” clouds. As expected, the CCEs reach longer lifetimes (up to more than an hour).

The split and merged cloud categories have the biggest maximum masses and radii. Some clouds in this category are the biggest clouds that lose some small fraction of their mass by splitting but remain relatively large, both in mass and area. The split and merged clouds mainly differ at the lower end of their cloud radii histograms as can be seen by the abundance of small-sized split clouds and hardly any small-sized merged clouds. The category characterized by the smallest maximum mass and radius is the proto clouds that did not undergo split or merge events. The CCEs are not amongst the largest clouds (in terms of both area and mass). This is due to two reasons. The first is that some of the largest clouds are formed by merging of two preexisting large clouds, none of which comprises more than 75% of the merged mass (our condition for CCE continuation). The second is that by the time the spin-up period is over, a few large split and merged type clouds already dominate the cloud field and are not part of our CCE collection (since CCEs initiate from proto clouds).

Two power law fits to the all-cloud type radii distribution were calculated: one for the small cloud radii subset and the other for the large cloud radii subset with a cutoff at 500 m. The slope of -1.21 for the small cloud subset is smaller than the previously reported range of -1.7 to -2 [Benner and Curry, 1998; G Zhao and Di Girolamo, 2007; Jiang et al., 2008; Dawe and Austin, 2012]. This may be due to our defined threshold of a minimum of four adjacent voxels (~ 110 m radius) that creates a general bias toward larger clouds (hence weaker slope). Moreover, the scale break (at 500 m) occurs at a smaller radius than previously reported. Nevertheless, the scale break radius and power law slope of the entire distribution (~ -2.3) are in agreement with recent work [Heus and Seifert, 2013].

Tracking a CCE is highly advantageous in that it enables us to follow a cloud along its whole life cycle, even if it undergoes minor merge and split events. Three examples of CCEs from the BOMEX-orig 500 cm^{-3} simulation are shown in Figure 3, two nonprecipitating and the other precipitating, for which the time evolution of cloud base and top heights, water mass COG (and COG of cloud droplets and raindrops), and buoyancy profiles from surface to cloud top are shown (see Appendix B for details on buoyancy calculations). The top and base heights are determined as the highest and lowest levels with $\text{LWC} > 0.005\text{ g kg}^{-1}$. The two nonprecipitating clouds represent two common pathways for cloud dissipation without precipitating—one which is nonreversible (Figure 3a) and one which is reversible (Figure 3b). The three CCEs were tracked for 38, 36, and 56 min. During the last 15 min of the precipitating CCE cloud lifetime, the cloud experienced significant precipitation below cloud base. Also indicated in Figure 3 are cases of splitting or merging (a total of 4, 3, and 12 cases for the nonreversible, reversible, and precipitating CCEs, respectively), which were found to be insignificant by the tracking algorithm, i.e., the CCE retained at least 75% of the total interaction mass.

Several interesting phenomena can be seen by following the CCE from beginning to end:

1. The cloud initially forms above a layer of positively buoyant air near the surface (red shading in Figure 3). It is stronger in the case of the deeper (precipitating) cloud, implying that the magnitude and time span of the initial buoyant plume may determine the cloud's future. Above it there is a negatively buoyant transition layer (blue colors near cloud base in Figure 3), which the updrafts manage to break through [Heus et al., 2009]. Generally, we found negative or neutral buoyancy near the cloud lifting condensation level (LCL) for all clouds, in agreement with previous studies that reported on this near-cloud base transition layer [Malkus, 1958; Garstang and Betts, 1974; de Roode and Bretherton, 2003; Grant and Lock, 2004; Neggers et al., 2007].
2. The cloud then develops and is maintained by one (in the nonprecipitating cases) or a series (precipitating case) of in-cloud positively buoyant plumes/thermals. These pulses were recognized in previous works [Blyth et al., 1988; Heus et al., 2009]. They span 5–15 min each.

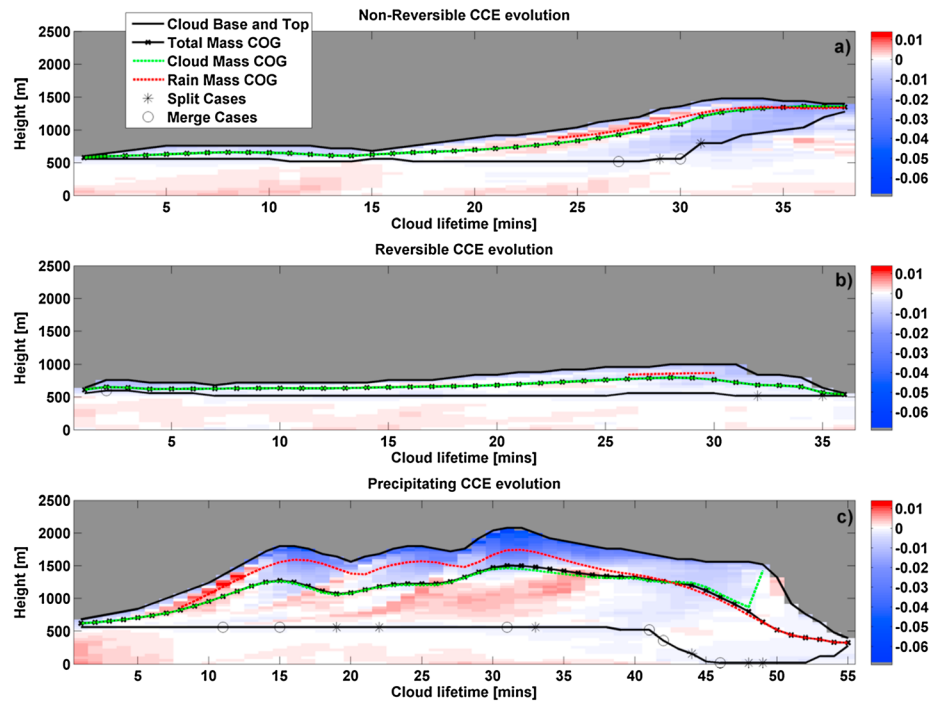


Figure 3. Time evolution of a representative (a) nonreversible dissipating, (b) reversible dissipating, and (c) precipitating CCE. The figure includes cloud base and top height (solid black lines), total water mass COG (solid crossed black lines), cloud water mass COG (dashed green lines), rain water mass COG (dashed red lines), and indications of insignificant splitting (asterisk markers) and merging (circle markers) events. Superimposed are mean surface to cloud top buoyancy profiles [m/s^2], where red (blue) shading corresponds to positive (negative) buoyancy. Note that for all cases the total mass COG initially follows the cloud droplet mass COG and at later stages (Figure 3c, once precipitation begins) total mass COG may follow the rain mass COG.

3. Cloud top regions consistently show negative buoyancy, due to overshooting of the level of neutral buoyancy or turbulent mixing with dry subsaturated environmental air and increased evaporation (cooling) [Squires, 1958; Blyth, 1993; Xue and Feingold, 2006].
4. Eventually, toward the end of the cloud lifetime, one of three scenarios may occur.
 - a For the nonreversible dissipating case, the CCE eventually decouples from the surface layer (i.e., negative subcloud buoyancy), and its base height increases as it dissipates by evaporation near the inversion layer. In this case the dissipation occurs from below. This is the most common scenario for BOMEX clouds.
 - b For the reversible dissipating case, at a certain point the cloud growth stops, but the CCE cloud base remains at the LCL. In this case the dissipation occurs from above, where both CCE mass and top height decrease with time. Frequently, clouds can undergo short periods of reversible dissipation followed by recoupling with a subcloudy layer thermal and reigniting of cloud growth (as seen in Figure 3c before precipitation begins) [Heus et al., 2009].
 - c For precipitating cases, significant rain mass accumulates at this stage. As shown in Figure 3c, the total mass COG follows the rain mass COG instead of cloud mass COG toward the end of the cloud lifetime, after which it precipitates. This stage is illustrated in Figure 3c by a decrease in cloud base height below the LCL until it reaches the ground, negative buoyancy profiles from the surface and through most of the cloud profile, and a fast decrease in total mass COG.

Although only three examples of CCE cloud evolution are shown here, they are representative of the main CCE evolutions in our simulations.

4.2. Analyzing the Evolution of All Clouds in the CvM Space

The locations of all clouds as sampled at all output time steps (every 1 min, over the course of 4 h of simulation, for the same simulation as in section 4.1) in the COG versus mass (CvM) phase space are presented in two scatterplots in Figure 4, one representing a morphological classification of clouds in the CvM space

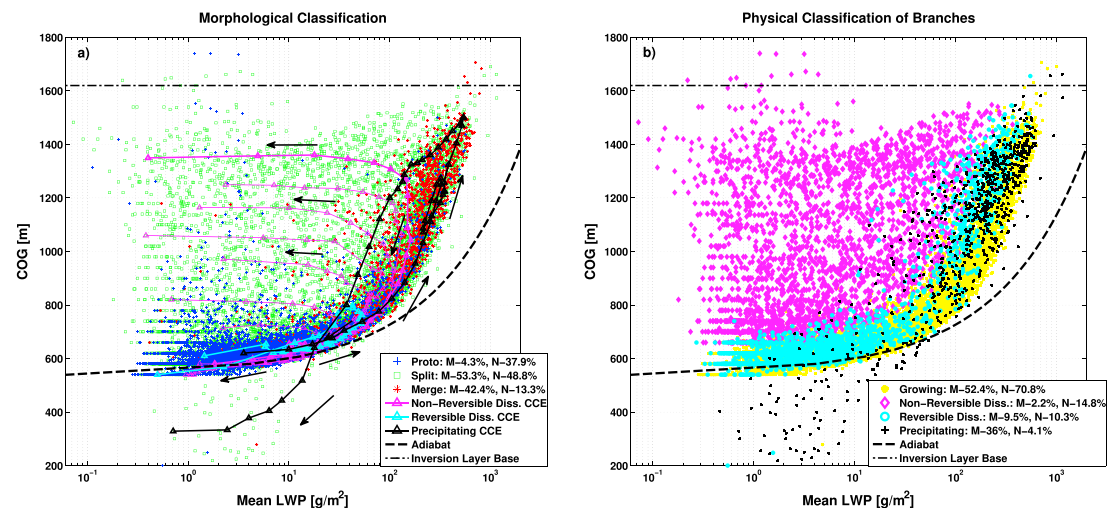


Figure 4. COG [m] as a function of LWP [g/m²] for all the clouds in the 500 cm⁻³ CCN BOMEX field (every 1 min over the course of 4 h of simulation). The adiabatic COG versus total column water mass estimation is shown by the black dashed lines, and the inversion layer base (after 5 h of simulation) is shown by the horizontal black dash-dotted lines. (a) Morphological classification, with blue markers representing proto clouds, red markers are for merged clouds, and green markers are for split clouds. The bold magenta, cyan, and black bold curves represent the three examples for the time evolution of specific nonreversible dissipating, reversible dissipating, and precipitating CCEs tracked in the domain, respectively (see Figure 3). Additional magenta lines represent other nonreversible dissipating CCE trajectories. Arrows indicate temporal evolution direction of CCE clouds in the phase space, with distances between markers for CCE clouds representing 1 min intervals. (b) Physical classification, with yellow markers representing growing clouds, cyan markers reversible dissipating clouds, magenta markers nonreversible dissipating clouds, and black markers precipitating clouds. Percentages of cloud samples and mass out of simulation totals for each cloud subset are indicated in the legends.

(Figure 4a), and the other representing a physical classification of clouds in the CvM space (Figure 4b). A single tracked cloud can be represented multiple times in this space according to its lifetime. The scatter in both plots is identical but labeled by different color coding which corresponds to additional information used. The information contained in both plots is purely complementary, as the morphological classification includes cloud-tracking (cloud history) information and the physical classification includes cloud growth, cloud base, and LCL information. The detailed definitions of the classifications will be given below in sections 4.2.1 and 4.2.2.

The X axes in Figure 4 correspond to mean cloud liquid water path (LWP [g m⁻²]) of all drop sizes, calculated by dividing cloud total mass by mean cloud horizontal area, so that a comparison with the theoretical adiabatic cloud LWP (black dashed line in Figure 4 corresponds to state after 5 h of simulation) can be performed. The adiabatic vertical profile was calculated by iteratively solving for the moist adiabatic parcel water content increase with height, using domain averaged temperature and pressure at the LCL height as the vertical profile initial conditions [Pontikis, 1996; Kostinski, 2008]. The inversion layer base height (black dash-dotted horizontal lines in Figure 4) after 5 h of simulation is also shown. It is important to note that COG represents the height where mass is concentrated and not the cloud's top height. For small mass clouds, where the cloud base and top are in close proximity, the COG may be a good representation of the cloud top height, but for large mass clouds the COG is located below the cloud top height.

Generally, it can be seen that the majority of clouds are confined between the adiabatic approximation curve and the inversion layer base. The small LWP and low COG clouds (correspond to initial stages of cloud formation) are located close to the adiabatic curve. However, as LWP increases (larger and deeper clouds), the scatter of clouds diverges from the adiabatic line. This is in agreement with subadiabatic expectations for most cumuliiform clouds [Warner, 1955]. Some large LWP clouds have COG above the inversion layer base, meaning that those clouds have tops that considerably overshoot the inversion layer base.

The representation in this CvM space provides a more realistic representation of the cloud evolution in comparison with simple parcel theory predictions or domain averages, as the full range of cloud trajectories is projected. As will be seen below, cloud field parameters such as effective cloudy layer top height (i.e., the

actual height to which many of the small dissipating clouds reach, as opposed to the theoretically calculated equilibrium level height), entrainment mixing magnitude/degree of adiabaticity (i.e., deviation of cloud growth trajectories from the adiabatic approximation), rain production, etc. can be deduced, making the CvM phase space an efficient map for describing cloud fields.

4.2.1. Morphological Classification in CvM Space

Different categories of clouds, as determined by the cloud-tracking algorithm (proto, merged, and split clouds), occupy specific subspaces in the CvM domain (Figure 4a). The locations of those subsets can be interpreted following the time evolution (trajectory) of a single CCE. Time evolution examples for the CCEs presented in Figure 3, the precipitating CCE (bold black line), reversible dissipating CCE (bold cyan line), nonreversible dissipating CCE (bold magenta line), are superimposed in Figure 4a. Additional nonreversible dissipating CCEs are plotted as well (magenta lines), to illustrate how the entire CvM domain can be occupied by evolving clouds.

A few stages in the CCE evolution can be identified along these example trajectories. The first stage is the growing stage, where clouds increase in both water mass and COG. Toward the end of the growing stage the cloud starts losing its water by evaporation (for the nonprecipitating clouds) and also by rain (for the precipitating cloud), and as a result its LWP decreases. It is important to note that the maximum mass and maximum depth (reflected by the COG) attained during the growing stage determine the rest of the trajectory of the CCE in the later dissipation stage, as is evident by observing the dissipating CCE trajectories. For the nonreversible cases, the dissipation trajectories appear as horizontal lines (depletion of cloud mass in time, with little change in COG), leaving small cloud remnants located above the adiabat and below the inversion layer base. For the reversible cases, the dissipation trajectories are similar to the growth trajectories (in proximity to the adiabatic curve) but the direction is opposite, with decrease in both COG and mass. Alternatively, some clouds manage to develop substantial precipitation, and after the growing stage they lose both COG and mass and often their COG falls below the adiabat (e.g., see thick black line, Figure 4a).

Considering these trajectories of representative CCEs, we can interpret the subspaces occupied by different groups of clouds. Added are corresponding cloud number and mass percentages for each group. The cloud number percent for a specific cloud type indicates the relative amount of points (clouds samples) in the CvM space attributed to that state, while the cloud mass percent indicates the relative amount of total simulation water mass attributed to that state. The proto clouds represent the initial stage in CCE life cycle (in case they later split or merge) or relatively small clouds throughout their entire lifetime. Proto clouds comprise 37.9% of all cloud samples, but only 4.3% of the total water mass in this simulation. For clouds that contain larger water mass and are more vertically developed, the likelihood of splitting (48.8% of cloud samples, 53.3% of mass) or merging (13.3% of cloud samples, 42.4% of mass) is higher compared to the small clouds.

The merged clouds mainly occupy the high-end LWP part of the CCE trajectory, where large growing clouds have a larger probability to merge with other clouds. The split clouds occupy the whole space as well as the upper limit of the biggest masses in the CvM space domain. The splitting events can create two or more resulting clouds, and thus the split clouds are the most widespread on the CvM phase space. For example, here 85%, 12%, 2%, and 0.4% of splitting cases result in 2, 3, 4, and 5 split clouds, respectively. Moreover, the clouds located below the adiabatic curve are mainly split type clouds that are precipitating segments of clouds.

4.2.2. Physical Classification in CvM Space

The insights obtained from the time evolution analysis (Figures 3 and 4a) propose an alternative classification scheme for the clouds in the CvM space, based on simple physical considerations. By comparing cloud base height (Cld_{base}) with the highest ($\text{LCL}(t)_{\text{max}}$) and lowest ($\text{LCL}(t)_{\text{min}}$) local (per column) LCL heights in the domain for a given time step, we may classify the clouds into four branches (see Figure 4b): (i) Growing branch, clouds with cloud base within the LCL limits ($\text{LCL}(t)_{\text{min}} \leq \text{Cld}_{\text{base}} \leq \text{LCL}(t)_{\text{max}}$). Additional term (for separating the growing clouds from dissipating clouds) is that growing branch clouds must increase either in mass or in top height compared to the previous cloud-tracking time step (1 min interval). (ii) Reversible dissipating branch, same cloud base criteria as the growing branch, but for clouds that decrease both in mass and in cloud top height compared to the previous cloud-tracking time step. (iii) Nonreversible dissipating branch, cloud base above the maximum LCL height ($\text{LCL}(t)_{\text{max}} < \text{Cld}_{\text{base}}$) and (iv) precipitating branch, cloud base below minimum LCL height ($\text{Cld}_{\text{base}} < \text{LCL}(t)_{\text{min}}$). The physical classification indeed separates the clouds in the CvM space into distinct subsets, where the main regions of overlap are along

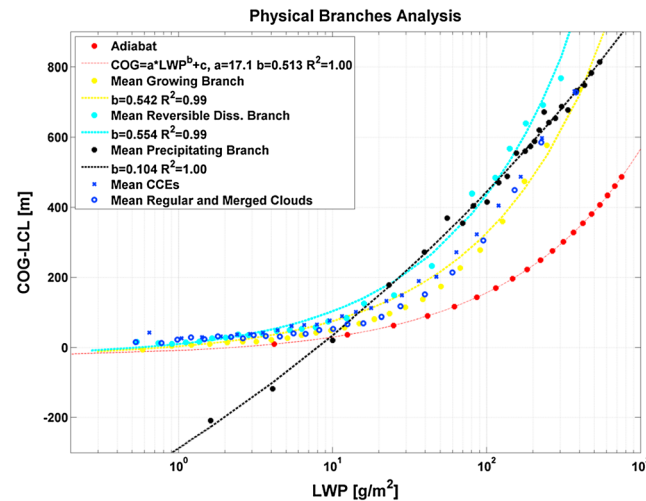


Figure 5. Mean COG-LCL [m] as a function of LWP [g/m²] for specific subsets in the CvM space, including: growing branch (yellow markers), reversible dissipating branch (cyan markers), precipitating branch (black markers), CCEs (blue cross markers), proto and merged type (blue circle markers), and the adiabatic approximation (red marker). Power law fits are added for the growing, reversible dissipating, and precipitating branches and the adiabatic (see legends for fit details).

ties, however, the separation to branches in the CvM space using this parameters is less unique with more overlap between the branches.

The morphological and physical classifications are complementary to each other and can be used to associate cloud types (from the cloud tracking) to physical stages in cloud lifetime. Most of the proto clouds are located around the initial and midparts of the growing branch (near the LCL) and in the lower regions of the dissipation branches. Merged clouds mainly occupy the high mass regions of both growing and precipitation branches, and split clouds occupy the entire phase space (all four of the branches). As opposed to what might be implied by the spatial distribution of clouds in the CvM space, the abundance of the clouds in each of the branches correlates poorly with the amount of total water mass they represent due to the logarithmic X axis. The growing branch comprises 70.8% of the cloud samples and 52.4% of the mass. The reversible dissipating branch comprises 10.3% of cloud samples and 9.5% of mass. The nonreversible dissipating branch comprises 14.8% of cloud samples but only 2.2% of the mass. Lastly, only 4.1% of cloud samples reside in the precipitating branch, but they constitute a significant part of the total mass (36%). The number asymmetry favoring growing branch clouds is in line with observations [Raubert *et al.*, 2007; Meerkötter and Bugliaro, 2009; Nuijens *et al.*, 2013] and numerical studies [M Zhao and Austin, 2005; Heus *et al.*, 2009; Plant, 2009; Witte *et al.*, 2014] of warm cumulus cloud fields, where for the majority of the clouds' lifetimes, cloud bases are at the vicinity of the LCL while cloud growth occurs.

4.2.3. Analysis of Branches in the CvM Space

Further understanding of the cloud field characteristics may be attained by in depth analysis of each of the branches (growing, reversible dissipating, nonreversible dissipating, and precipitating). Out of the four, the growing and reversible dissipating branches are most intuitive to physically interpret since they can be easily compared with a (sub)adiabatic parcel model. In Figure 5 the mean curves representing the growing branch (yellow markers) and reversible dissipating branch (cyan markers) are compared with the adiabatic approximation (red markers). Based on physical considerations, the curves can be well represented by a power law (see Appendix C for details):

$$\text{COG} = a \text{LWP}^b + c, \quad (2)$$

where a is a function of the b coefficient and environmental conditions (i.e., cloud base thermodynamic properties, see equation (C5)), c is the LCL height, and b is a measure for the liquid water content (LWC) dependence on height (i.e., $\text{LWC} \propto H^{1-b}$, $0.5 < b < 1$). The values for b range between 0.5 in the case of adiabatic cloud to 1 in the extreme case of fixed LWC with height (see Appendix C). By using COG-LCL as our vertical

the growing and reversible dissipating branches and especially the large LWP, high COG region, where clouds may either be growing, precipitating, or at the high mass end of the dissipating cloud branches.

We note that the physical classification above can be tightly linked to other cloud parameters. One such an example is cloud vertical velocities. Growing branch clouds typically experience updrafts at the cloud base and positive average vertical velocities for the entire cloud. Nonreversible dissipating clouds show the opposite, with downdrafts at cloud base and negative average velocities. Reversible dissipating clouds show updrafts at the cloud base and neutral average velocities, while precipitating clouds show downdrafts at the cloud base and neutral average velocities. Due to large variance of vertical velocities,

coordinate we can eliminate the c coefficient. The adiabatic curve perfectly matches the power law: $\text{COG} \propto \text{LWP}^{0.513}$. The LWP exponent is slightly above 0.5, meaning that the explicit moist adiabatic LWC increase is slightly sublinear (i.e., linear increase of LWC with height yields an exponent of 0.5).

Using a coefficient from the adiabat power law fit, we can solve equation (C6) to obtain the domain specific thermodynamic constant, γ , and use it to constrain power law fitting for the other branches in the domain, so that COG is only a function of the LWC dependence on height (b), namely

$$\text{COG} = f(b) \text{LWP}^b$$

$$f(b) = \frac{\left(\frac{1}{b}\right)^{1+b}}{\frac{1}{b} + 1} \rho \gamma^{-b} \zeta^{1-b} \quad (3)$$

where $\zeta = 1 \times 10^{-3}$ [m] is a constant vertical scale, and $\rho = 1$ [kg/m³] the air density. It is seen that the power law also applies for the mean of the growing branch but has a larger exponent $b = 0.542$, indicating subadiabaticity of the cloud field (i.e., $b > 0.513$ implies sublinear LWC increase with height for the BOMEX case). Both mixing with dry air and water loss via precipitation can contribute to lower LWC with height and subadiabaticity. Hence, the exponent of the power law may be used as a direct measure for the degree of adiabaticity of the cloud field. As expected due to further deviation from the adiabat, the mean of the reversible dissipating branch corresponds to a slightly larger (and less adiabatic) exponent $b = 0.554$. This branch can be considered as a subadiabatic pathway back to a similar location of the early cloud growth stages.

For cases where the growing branch is less pronounced (e.g., when high precipitation efficiency maintains a cloud base lower than the LCL, as will be seen in Part II), alternative subsets of cloud types may be taken to represent the growing stages of clouds. The mean of the CCEs (blue crosses) and mean of the proto and merged type clouds (blue circles) are compared with the mean growing branch curve. Both mean curves compare well with the growing branch, with a slight overestimation of the COG (more so for the CCE curve). This is due to the addition of mainly nonreversible dissipating branch clouds to the averaging, which by definition have higher COG than the growing branch for the same mass.

The mean of the precipitating branch (black markers, Figure 5) is also plotted. It can also be well represented by a power law, with an exponent $b = 0.104$. As opposed to the case of the growing branch, the physical interpretation of the exponent value (and other fit coefficients) is not straightforward, as theory predicting the decrease of COG with decrease of LWP due to precipitation has yet to be developed. It is likely that the precipitating branch reflects a superposition of growth, dissipation, and sedimentation processes. This assumption is supported by Figure 5, where the precipitation branch coincides with the growing branch at high masses, reversible dissipation branch at intermediate masses, and falls below the adiabatic approximation at the lowest masses.

Nevertheless, the power law exponent serves as means of comparing with other branches and other domains. Further analysis shows that the abundance of precipitation branch clouds below the adiabat is indicative of the rain amount reaching the surface, while the abundance of precipitation branch clouds above the adiabat is mainly indicative of precipitation processes in the clouds (see section 4.3.1).

Unlike the growing, reversible dissipating, and precipitating branches, which are relatively confined in the CvM space, the nonreversible dissipating branch is much more disperse and fills most of the space between the growing branch and the inversion layer base height. However, from Figure 4a it is clear that a consistent nonreversible dissipation pathway behavior exists. Following CCE trajectories in the CvM space reveals that the pathway of a cloud in the nonreversible dissipation area is directly linked to its maximum COG in the growing branch.

In Figure 6a, a normalized density plot of the nonreversible dissipation branch is shown. The low LWP-low COG region is a preferred location for nonreversible cloud dissipation, meaning that most clouds that form here fail to develop substantially, as can also be seen for the reversible dissipating branch. This is in line with a general gradual decrease in abundance of dissipating clouds with increasing COG. For higher levels of COG the dissipating space is smoothly occupied, indicating that dissipation pathways occur at all heights within the cloudy layer. We note that a bimodal pattern is seen, with a second local peak of dissipating cloud abundance at $\text{COG} \sim 1250$ m due to convergence of nonreversible dissipating pathways slightly below the inversion layer base.

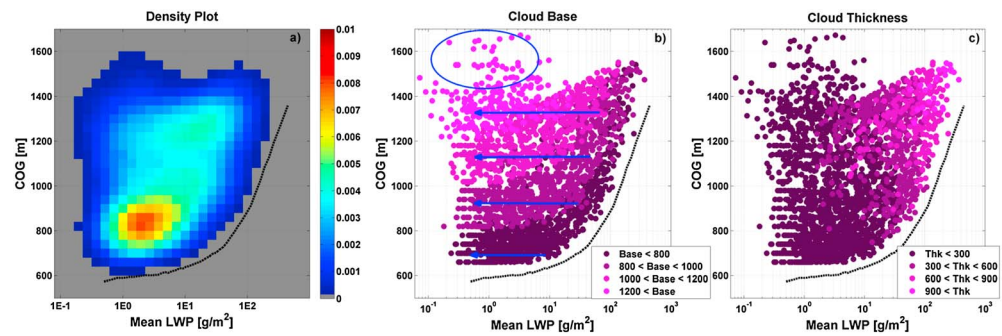


Figure 6. Nonreversible dissipating branch cloud analysis in the CvM space. (a) Normalized density plot. (b) Clouds sorted by base heights values, as described in panel legend. Blue arrows represent CCE nonreversible dissipation pathways as seen in Figure 4a. Clouds within the marked ellipse likely form by a shedding mechanism as described in the text. (c) Clouds sorted by vertical thickness, as described in panel legend. Black dashed lines show the average growing branch location.

Figures 6b and 6c sort the nonreversible dissipation branch by cloud base height and cloud thickness, respectively. As a first approximation, the cloud thickness can be taken as proportional to the cloud mean LWP, for all COG heights. The distribution of dissipating cloud base height is less straightforward. The distance between a dissipating cloud and the growing branch on the CvM space can be linked (nonlinearly) to the cloud base height; the larger the distance, the higher the base height. For small LWP ($<10 \text{ g m}^{-2}$), almost all clouds are of small sizes, with cloud depth less than 300 m and a COG nearly equal to cloud base height (i.e., strong cloud base height dependence on COG height). As we move to larger LWP, cloud base height tends to be constant with COG height (i.e., strong cloud base height dependence on LWP).

Added to Figure 6b are schematic nonreversible dissipation pathways (blue arrows), as inferred from the nonreversible dissipation pathways of CCEs in Figure 4a. They are manifested in the CvM space by loss of cloud mass with little change in COG. From Figure 3a it was seen that such a pathway represents dissipation by rising cloud base. The gradual increase in cloud base (Figure 6b) and decrease in thickness (Figure 6c) with decreasing LWP are consistent with Figure 3a, implying that the majority of nonreversible dissipating clouds follow the rising cloud base dissipation pathways. Nevertheless, the highest COG nonreversible dissipation branch clouds (encompassed by the blue ellipse in Figure 6b) seem to stand alone. They are unlikely to form by gradual dissipation since no clouds with similar COG height but larger LWP values exist for them. Using cloud-tracking data, we found that these clouds form by a shedding (splitting) mechanism of small mass and high COG clouds from large well-developed clouds. This shedding also occurs at other regions with prominent negative buoyancy. Such an example is frequent shedding of small mass and low COG clouds near the cloud base, but in that case the clouds cannot be distinguished since they are intermixed in the CvM space with other clouds that follow rising base dissipation pathways.

4.3. Comparison of Simulations in CvM Space

4.3.1. Full CvM Space Comparison

We now review a selection of simulations and see how meteorological conditions are manifested in the CvM space. Four different simulations (BOMEX-org, BOMEX-lowinv, BOMEX-highinv, and AMAZON, as described in section 2) are presented on the CvM space (Figure 7), using both classification types. In addition, for precipitating branch subsets only, specific thermodynamic parameters that cannot be explicitly inferred from the CvM space are compared in Table 1. The simulations were initialized using different thermodynamic profiles and with the same initial concentration of aerosol (500 cm^{-3}). Similar to Figure 4, the adiabatic estimations and inversion layer base heights are added for reference (after 5 h of simulation). Figures 7a–7c and 7e–7g show the effect of modifying the cloudy layer depth (by changing the inversion layer height) on the cloud development in the BOMEX case studies. We note that the BOMEX thermodynamic profiles change very little (i.e., differences between profiles remained much larger than changes along time per profile) throughout the 8 h of simulation, while the AMAZON simulation profile showed slight warming and a gradual increase of $\sim 50 \text{ m}$ per hour in the LCL height.

In all three BOMEX simulations there are only minor differences in the total number ($\sim 17 \times 10^3$) of tracked clouds and number and mass fractions of different cloud morphological types, indicating that the changes

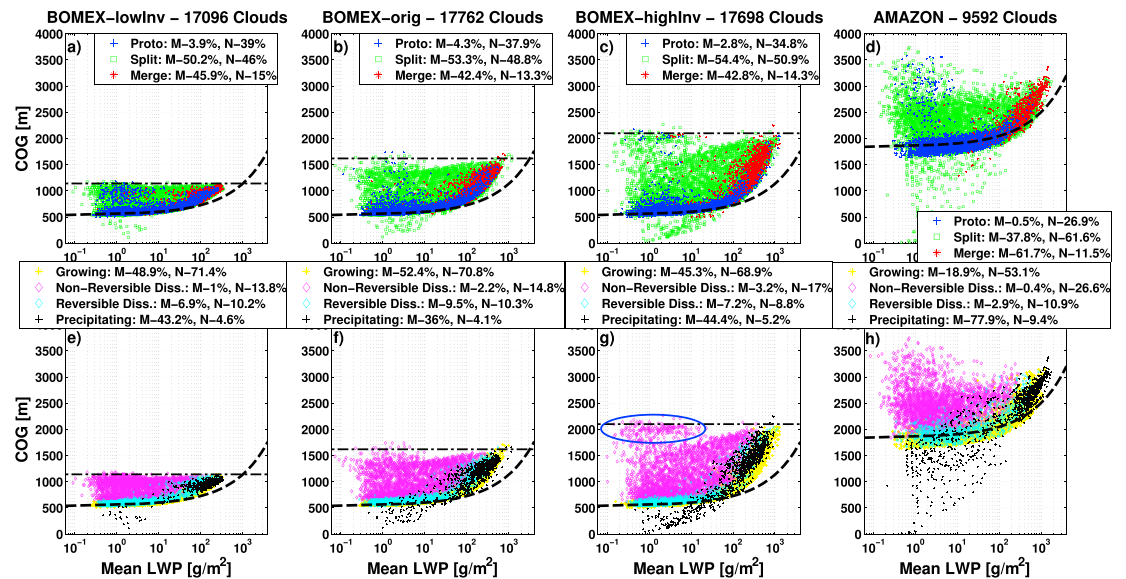


Figure 7. Same scatterplot of clouds in the CvM space as presented in Figure 4 for four different case studies, showing both morphological (a–d) and physical (e–h) classifications of the clouds. Case study names and total tracked cloud amounts are included in upper panel titles and correspond to the case studies described in section 2. All cases were run with 500 cm^{-3} aerosol concentrations. AMAZON profile does not have a distinct inversion layer (see Figure A1), so its inversion base height is not included.

in inversion layer height has little effect on the cloud field organization and interactions between the clouds. Proto clouds comprise less than 2–5% of the mass but 35–40% of the cloud samples. Split clouds comprise 50–55% of the mass and 45–50% of the samples, and merge clouds comprise 40–45% of the mass and 13–15% of the samples.

For the BOMEX-lowinv simulation (Figures 7a and 7e inversion at $\sim 1000 \text{ m}$), the scatterplot presents a thin cloudy layer, where proto clouds (together with merged and split clouds) manage to occupy almost the entire growing branch. The growing branch consists of about half of the mass (48.9%) and the majority of cloud samples (71.4%) in this simulation. The reversible dissipating branch (6.9% of mass, 10.2% of samples) covers most of the growing branch, excluding the highest masses. The nonreversible dissipating branch (only 1% of mass, 13.8% of samples) fills most of the space between the adiabatic curve and the inversion layer base and is densely populated by split clouds and to a lesser degree proto clouds that form within the cloudy layer. The cloudy layer is shallow in this case and little effect of entrainment is seen, i.e., the growing branch is close to the adiabatic curve. This small effect of the entrainment process on the clouds can be explained by the high relative humidity values in the shallow cloudy layer in this simulation (see the profile in Figure A1). Although yielding little surface precipitation (total of $\sim 46 \text{ mm}$), a significant amount of mass can be attributed to the precipitating branch (43.2% of mass, 4.6% of samples), indicating that a few of these relatively shallow cumulus clouds can grow to very large sizes and be rather efficient at producing precipitation.

For the BOMEX-orig simulation (Figures 7b and 7f inversion at $\sim 1500 \text{ m}$) there are higher COG values compared with the BOMEX-lowinv simulation, representing a deeper cloudy layer and larger cloud masses.

Table 1. Selected Cloud-Tracking Parameters for Precipitating Branch Subsets^a

Case Study	$A_{\text{mean}} (\text{km}^2)$	Thk (m)	$W_{\text{max}} (\text{m s}^{-1})$	$\text{LWC}_{\text{max}} (\text{g m}^{-3})$	ACP (mm)
BOMEX-lowinv	1.20 ± 0.61	1167 ± 226	3.05 ± 1.19	1.41 ± 0.46	46.49
BOMEX-orig	1.00 ± 0.73	1472 ± 450	3.62 ± 2.23	1.40 ± 0.82	89.52
BOMEX-highinv	0.92 ± 0.54	1747 ± 641	4.12 ± 2.64	1.43 ± 0.89	177.43
Amazon	2.93 ± 4.25	2244 ± 1300	5.33 ± 3.81	1.46 ± 1.21	723.93

^aParameters include (from left to right) cloud mean horizontal area, thickness, maximum vertical velocity, maximum liquid water content, and domain accumulated surface precipitation. Values represent simulation time averages and corresponding standard deviations.

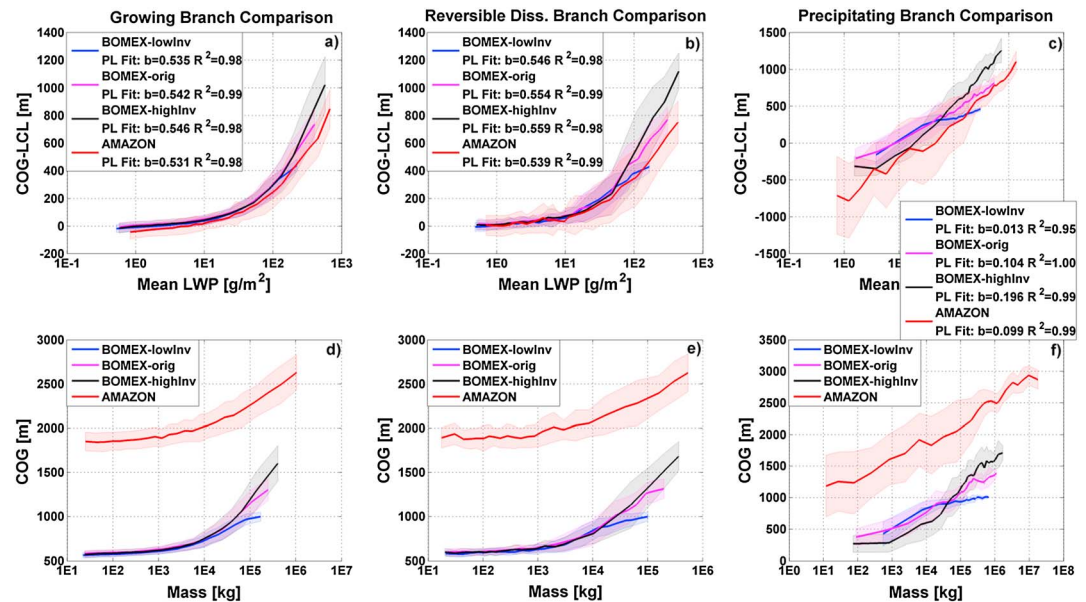


Figure 8. Comparison of mean growing (panels a, d), reversible dissipating (panels b, e) and precipitating (panels c, f) branch curve for the BOMEX and AMAZON simulation, as seen in Figure 7. Data are sorted either by mean cloud LWP [g/m^2] with (a–c) COG-LCL [m] Y axes or by total water mass [kg] with (d–f) COG [m] Y axes. Solid lines represent the mean curves, and shades the standard deviations, with different colors representing different simulations (see panel legends). Power fit exponents and goodness of fit (R^2) are included in Figures 8a–8c legends as well.

There is also a noticeable deviation of the growing branch from the adiabat at large masses. This is accompanied by the larger deviation of the reversible dissipating branch from the growing branch as well. Only a small portion of small mass clouds ($\text{LWP} < 10^2 \text{ g/m}^2$) have COG above the inversion layer, while many of the large mass clouds reach the inversion layer and some even overshoot it (top height significantly above the inversion base height). Although the number of precipitating clouds below the adiabat increases (as does the amount of surface rainfall – total of $\sim 89.5 \text{ mm}$), the total percent of precipitating branch clouds remains unchanged and the percent of mass attributed to the precipitation branch decreases (36%) compared to the BOMEX-lowInv case. This is compensated by minor mass increases of a few percent in the other branches.

The BOMEX-highInv simulation (Figures 7c and 7g inversion at $\sim 2000 \text{ m}$) results present a continuation of the trends described above. This simulation produces clouds with higher COG and larger mass, exhibits a larger deviation of the growing branch and reversible dissipation from the adiabat, and more low COG precipitating clouds and surface precipitation (total of $\sim 177 \text{ mm}$), but with only minor changes in the relative distribution of mass and number between the branches compared to the other BOMEX simulations. The nonreversible dissipation branch in this simulation is clearly divided into two separate regions, one which extends from the growing branch to smaller mass and one near the inversion layer base (enclosed within the blue ellipse in Figure 7g). As described in section 4.2.3, the former mainly represents gradual dissipation of clouds via a rising cloud base, while the latter mainly represents shedding of small clouds from the tops of deep clouds.

According to the analyses, two indications for the magnitude of entrainment can be derived from the CvM phase space. The first is the deviation of the growing branch from the adiabatic approximation. This deviation, however, is similarly affected by entrainment and sedimentation; and thus, entrainment effects should be examined only on growing branch clouds that mainly consist of cloud droplets with negligible terminal velocity (i.e., more polluted cases or clouds in their early development stages). The second indication of entrainment is the number of clouds that their COG reaches the inversion layer base for all LWP values. Less entrainment in the cloudy layer would enable the clouds to fulfill their convective potential and reach the inversion layer (and above, since COG height is equal or lower than cloud top height). In the dissipation stage less entrainment decreases the rate at which clouds evaporate [Dagan *et al.*, 2015; Lu *et al.*, 2015]. In the CvM space this effect would be manifested by clouds fully occupying the region delineated between

the adiabat and the inversion layer base. Indeed, in the BOMEX-lowinv simulation we see a dense population of clouds near the inversion layer base since the cloudy layer is thin and characterized by relatively high RH values. In the two other BOMEX simulations the cloudy layers are thicker, and the RH decreases with increasing height, thus fewer clouds manage to reach the inversion layer.

The Amazon simulation (Figures 7d and 7h) differs greatly from the BOMEX ones. The higher temperature and lower humidity near the surface over land result in a much higher LCL (~ 1.5 km, ~ 1 km higher than in the BOMEX case). As seen for other case studies, the theoretical LCL predicts the simulated cloud base accurately during the course of the simulation. Even though this case lacks an inversion layer, results show that the effective cloudy layer top height can be set at ~ 3.5 km. The effective cloudy layer top in this case is determined by a combination of increased entrainment and gradual profile stabilization above the LCL height. The growing branch appears to deviate less from the adiabatic approximation in comparison with the BOMEX cases and reaches higher mass values. It is also considerably wider than in the BOMEX cases, probably due to the twofold increase in cloud LCL height variance for that simulation. This may also partially explain the increased variance of the precipitating branch scatter per LWP value. The reversible dissipating branch also shows much larger variance per LWP compared to the BOMEX cases, with much more overlap with the nonreversible dissipating branch region. The nonreversible dissipating branch bears similarity to the BOMEX-highinv one, where the protruding segment of high COG and low mass can be considered separate from the lower dissipating clouds, due to different mechanisms of their formation.

A major difference between the AMAZON and BOMEX simulations is how the mass and number of clouds are distributed in the different cloud types and physical branches. Proto clouds only comprise 0.5% of the mass but 26.9% of the cloud samples, split clouds 37.8% of the mass and 61.6% of the cloud samples, and merged clouds 61.7% of the mass but only 11.5% of the cloud samples. The dominance of merging events is clearly reflected in the threefold larger cloud sizes of the AMAZON precipitating branch clouds. More dramatic is the increase in mass attributed to the precipitating branch (77.9% of mass) in expense of the growing branch (18.9% of mass), with increased surface precipitation (total of ~ 723 mm) which lowers the cloud base. The increased precipitation can be explained by larger cloud sizes and thicknesses, vertical velocities, and slightly larger LWC, as seen in Table 1. The results above indeed show that the abundance of clouds whose COG lie below the adiabatic curve is a good indicator of surface rain amounts, and that the well-known relationship between cloud thickness and surface rain holds in the simulations.

4.3.2. Mean Cloud Pathways in CvM Space

The fact that subsets in the CvM space occupy well-defined regions enables us to average these subsets and compare mean subset curves for different simulations instead of comparison of the entire occupied CvM space. As seen in Figure 5, these subsets may include among others the mean growing, reversible dissipating, or precipitating branches, mean of CCEs trajectories, or mean of proto and merged type clouds. This analysis enables easy and direct comparison between different fields or different model results. In Figure 7 mean cloud LWP was used to represent the cloud mass in the CvM space, mainly for easy comparison with the adiabatic approximation. However, when comparing mean curves, averaging can be done with respect to either LWP or total mass. The former is advantageous for comparisons with cloud parcel theory and is a good measure of cloud thickness but is disadvantageous in that clouds of vastly different total masses (i.e., different areas, shapes) are considered together. For this reason, results here are shown for both methods of averaging.

Figures 8a–8c present the mean growing, reversible dissipating, and precipitating branch curves for the BOMEX and AMAZON simulations, respectively, with averaging by LWP [g/m^2] and with Y axes set as in Figure 5 (COG–LCL [m]) for best power law fitting results. Figures 8d–8f show the same data but averaged by total water mass [kg] and with COG [m] on the Y axes. The clear differences seen between the curves on the CvM phase space point to the different average properties of the branch clouds driven by the different thermodynamic conditions, as these are all simulations with 500 cm^{-3} aerosol concentrations. The standard deviation for each curve (shaded areas in Figure 8) indicates the spread of clouds around the mean curve or thickness of the branches.

First comparing the mean growing branch curves, it can be seen that all three BOMEX simulations have almost identical mean curves for small and medium masses, with very small standard deviation values. For

large masses ($LWP > 10^2$, total mass $> 10^5$), raising or lowering the inversion base height of the original BOMEX profile results in corresponding shifts in their mean CvM trajectories, with maximum COG higher (lower) by ~ 300 m for the higher (lower) inversion shift. Increasing the inversion base height also drives an increase in the maximum mass of the curves and the COG standard deviation per mass value. Power law fit exponents (legend, Figure 7a) increase with higher inversion layer height (from 0.535 to 0.546), indicating a corresponding decreased level of adiabaticity.

For the AMAZON case, when averaged by COG-LCL versus LWP, the curve bears similarity to the BOMEX ones, with a slightly lower trajectory. But when averaged by COG versus total mass the mean curve is located well above the BOMEX ones and reaches 5 times the maximum cloud mass, indicating much larger cloud areas (as seen in Table 1). The AMAZON curve in Figure 8a shows a higher level of adiabaticity (power law exponent of 0.531), even though the AMAZON thermodynamic profile has slightly lower relative humidity in the cloudy layer in comparison with BOMEX. This may be due to the significantly larger cloud sizes and thicknesses for the AMAZON case (see Table 1) that reduce the influence of entrainment on the clouds, and due to larger maximum vertical velocities and larger cloudy layer buoyancy (not shown here) that promote higher LWC, together yielding more adiabatic conditions.

The mean reversible dissipation curves (Figures 8b and 8e) bear great resemblance to the mean growing branch curves. This can be expected since they basically consist of similar CvM trajectories but of reverse directions. As indicated in Figures 5 and 8, the mean reversible dissipation curves are less adiabatic than the mean growing branch, with power law exponents ranging from 0.546 (lowInv) to 0.559 (highInv) for the BOMEX simulations and 0.539 for the AMAZON simulation. The rank of adiabaticity seen for the mean growing curves is maintained for the mean reversible dissipation curves as well. Two additional differences between the two branches are that the reversible dissipation branch reaches lower maximum mass values and exhibits larger standard deviations per mass value, as expected from the larger CvM scatter seen in Figure 7.

The precipitating branches (Figures 8c and 8f) for BOMEX simulations show opposite behaviors for small and large cloud masses, with a common crossover point at medium mass values. At large masses, the higher the inversion layer height, the higher the precipitating branch extends. At small masses, the higher the inversion layer, the lower the precipitating branch extends. When compared in the COG-LCL versus LWP space, the AMAZON precipitating branch most resembles the BOMEX-orig case but extends to both lower and higher masses. The large span of the branch is more obvious in COG versus total mass space. A few conclusions can be reached from the precipitating branch analysis and from accumulated surface rain data (see Table 1): (i) the branch slope (Figure 8c) is not necessarily indicative of surface rain amounts. (ii) The lower the branch extends below the LCL height, the more surface rain can be expected, and (iii) the large span of mass and branch standard deviation values is an additional indication of surface rain.

5. Summary

A new 3-D cloud-tracking algorithm is introduced. The algorithm tracks the evolution of individual clouds including identification of splitting and merging cases, with the ability to track the evolution of Continuous Cloud Entities (CCE) along their whole lifetime while they go through insignificant merge and split events and keep their identity. The altitude of the cloud center of gravity (COG) and its total mass (or mean LWP) is calculated for each cloud and projected on the COG versus Mass (CvM) phase space at 1 min temporal resolution. Each cloud creates a trajectory in the CvM space due to its mass and COG evolution in time. The projection of all the clouds in a given field (defined by the initial thermodynamic conditions and aerosol loading) on the CvM phase space or averaging it into a mean curve is a useful and compact way to examine the cloud field properties. Hence, we propose to use this space as a general map for describing cloud fields.

By observing typical CCE trajectories, one can link basic processes during the cloud lifetime to the different regions in the CvM phase space. The majority of clouds originate at COG near the lifting condensation level (LCL) height with small mass values (i.e., bottom left subspace) and then increase in both mass and COG altitude. After growing to some maximum mass, a cloud may reside some time at the mature stage and sometimes start to precipitate (with no significant changes in COG or mass), followed by the dissipation stage, where there are three main possibilities (see Figures 3 and 4). 1. *Nonreversible dissipation*: The cloud

evaporates mainly from the lower part of the cloud accompanied by rising cloud base, showing reduction in mass without much change in COG (see the low mass-high COG part of the nonreversible trajectories in Figure 4a). 2. *Reversible dissipation*: The cloud evaporates mainly from the upper part of the cloud accompanied by a decrease in cloud top, showing simultaneous decrease of COG and mass in the CvM space. These clouds eventually return close to the cloud's initial state on a trajectory nearly identical (but in opposite direction) to cloud growth. 3. *Precipitating*: The cloud simultaneously loses mass and COG with a lowering of the cloud base, where initially the loss of mass is dominant and toward the end of the cloud lifetime the decrease in COG is dominant.

These insights, combined with cloud-tracking information, enable morphological and physical classifications of the CvM subspaces. The morphological classification partitions the space according to the cloud type (proto-new cloud, split cloud created by splitting event, merged cloud created by merging event), while the physical classification partitions the space according to cloud base height with respect to the LCL, yielding growing and reversible dissipating (for cloud base near LCL), precipitating (for cloud base below LCL), and nonreversible dissipating (for cloud base above LCL) branches. The additional separation between the growing and reversible dissipating branches is done based on the condition that growing branch clouds must increase either in mass or cloud top with respect to their previous state. The distribution of cloud amount and total water mass within each subset gives information as to which cloud type/process dominates the cloud field. The growing, reversible dissipating, and precipitating branches can both be represented by a power law $\text{COG} \propto \text{LWP}^b$ that enables easy comparison between different simulations. In the case of the growing and reversible dissipating branches, the power law exponent can be physically interpreted and directly compared with the ~ 0.5 value (corresponds to the purely adiabatic case) to test degree of adiabaticity. Analysis of the nonreversible dissipating branch clouds shows that they reach the low mass—high COG regions either by gradual dissipation of cloud mass while their cloud base rises or by shedding of small clouds off larger clouds.

We have shown that the CvM space is a useful tool for comparison between different simulations. These comparisons may be done using either the entire CvM space (Figure 7) or averages of specific CvM subsets (Figure 8). In the latter case, there are multiple choices for which subset to average, depending on what process we are aiming to compare, and on the specific characteristics of the simulation. Moreover, averages can be done with respect to total mass or LWP in the X axis, and COG or COG-LCL in the Y axis, each contributing information on the cloud field. For example, in Figure 5 we see that the averages of the growing branch clouds, proto + merged clouds, and CCEs are all similar to each other. Thus, in cases when the growing branch (or any other branch or subset) is less prominent or cannot be easily defined, alternative options may exist.

Using BOMEX as our main case study, we have shown that an increase in the cloudy layer depth decreases the degree of adiabaticity (as the RH values decrease toward the top of the cloudy layer) and increases the amount of surface rain, without generating major changes in the partition of clouds between the different morphological and physical classification types. Amazonian clouds show a higher degree of adiabaticity in spite the lower levels of relative humidity below and within the cloudy layer, probably due to significantly larger sizes (both horizontal and vertical) and vertical velocities in those clouds. As a direct continuation to the findings here, in Part II of this work we use the CvM space as a main tool to analyze the effects aerosols have on BOMEX clouds.

Appendix A: Case Study Setups

As described in section 2, four different thermodynamic initializations were used in this work: three BOMEX profiles and one Amazonian profile. The skew-T plots of all profiles are illustrated in Figure A1 below. Up to a pressure level of ~ 910 hPa, all three BOMEX profiles are identical. The initial Amazon profile yields much higher LCL (1.4 km) than the BOMEX profile and increases during the course of the simulation (up to 1.8 km after 8 h).

Surface fluxes and stress velocity used to initialize the simulation are shown in Table A1. The initial profiles do change slightly with simulation time. To maintain relatively stable thermodynamic conditions, we use large-scale forcing for the BOMEX simulations (see appendix of [Siebesma et al., 2003] for details) and nudging (with a 15 min time scale tested for producing stable runs) for the Amazon simulation.

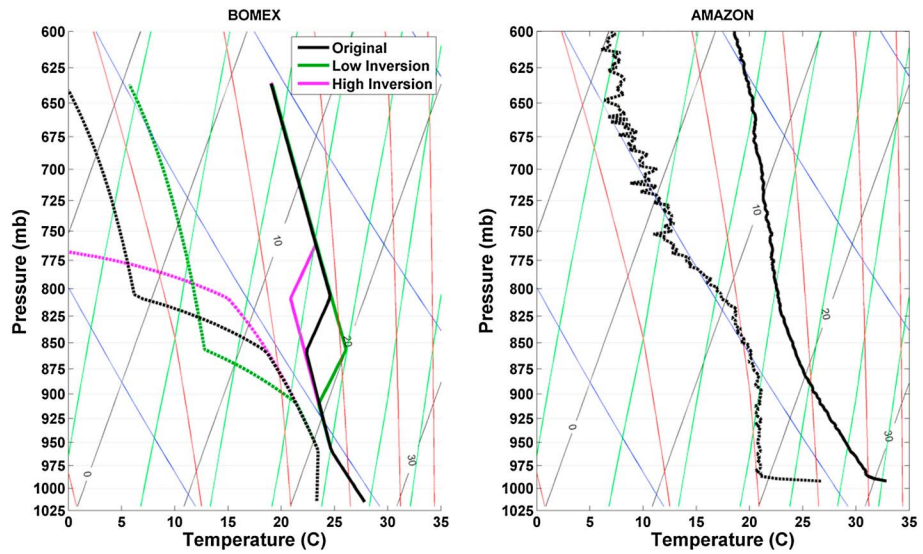


Figure A1. Skew-T plots of different soundings used to initialize SAM model in this work. Bold lines represent sounding temperature (solid) and sounding dew point temperature (dashed). Thin lines represent isotherms (black), constant mixing ratio (green), dry adiabats (blue), and moist adiabats (red). For full interpretation of skew-T, see http://www.atmos.millersville.edu/~lead/SkewT_HowTo.html.

Appendix B: Cloud-Tracking Details

Tracked cloud buoyancy vertical profiles were calculated based on the equation:

$$B = g \left[\left(\frac{\theta' - \bar{\theta}}{\bar{\theta}} \right) + 0.61 (q'_v - \bar{q}_v) - q_l \right], \quad (B1)$$

where B [m/s^2] is the buoyancy, θ is the potential temperature, q_v the vapor mixing ratio, q_l the liquid water mixing ratio, and g the gravitational constant. For each cloudy vertical level, the cloud horizontal cross-section averages (denoted by $'$ in equation (B1)) were compared with noncloudy domain averages (denoted by $\bar{\cdot}$ in equation (B1)). For subcloudy vertical levels, the horizontal cross section shaded by the cloud base was compared with the rest of the domain.

The variables saved by the cloud-tracking algorithm are listed in Table B1.

Appendix C: Analytical Expression for COG Dependence on LWP

Here we propose an analytical expression for cloud COG versus LWP without explicitly solving the moist adiabatic vertical profile. It is based on the assumption that for adiabatic clouds the cloud liquid water content (LWC [g/m^3]) is linearly dependent on height [Pontikis, 1996] and cloud base characteristics. The liquid water path (LWP) in the adiabatic case is

$$\text{LWP} \left[\frac{\text{g}}{\text{m}^2} \right] = \int_0^H \text{LWC} dz = \int_0^H \rho \gamma \frac{z}{\zeta} dz, \quad (C1)$$

where ρ [$\frac{\text{kg}}{\text{m}^3}$] is the air density, γ [$\frac{\text{g}}{\text{kg}}$] is a constant mixing ratio increase magnitude depending on cloud base temperature, saturation mixing ratio, and thermodynamic constants, with typical values ranging between 1 and 2.5×10^{-6} [$\frac{\text{g}}{\text{kg}}$], and ζ [m] is a corresponding constant length scale for LWC increase, typically 1×10^{-3} . Here we consider H as the cloud depth with respect to the cloud base. A more general expression should take into consideration the fact that clouds are subadiabatic [Khain et al., 2013], with the upper bound being the adiabatic case. In such a case one should expect a sublinear increase of LWC with height.

Table A1. Surface Properties for the Simulations in This Work

Case Study	Surface Temperature (K)	Sensible Heat Flux (W/m^2)	Latent Heat Flux (W/m^2)	τ (m^2/s^2)
BOMEX	301	9.46	153.4	0.0784
Amazon	304.25	131	340	0.28

Table B1. List of Saved Variables for Each Tracked Cloud

Cloud Tracking Variable	Units	Notes
Base	m	-
Top	m	-
Simulation time	hh:mm:ss	-
CCOG: cloud droplet center of gravity	m	-
Variance around CCOG	m	-
RCOG: rain center of gravity	m	-
Variance around RCOG	m	-
Cloud mass	kg	^(a)
Rain mass	kg	^(a)
Volume	km ³	^(a)
Surface area	km ²	-
Mean horizontal cross-sectional area	km ²	-
Maximum horizontal cross-sectional area	km ²	-
Shaded horizontal cross-sectional area	km ²	-
Liquid water content (LWC)	g m ⁻³	^(a,b)
Mean vertical velocity (<i>W</i>)	m s ⁻¹	^(a,b)
Maximum <i>W</i>	m s ⁻¹	-
Mean cloud base <i>W</i>	m s ⁻¹	-
Mean lifting condensation level (LCL) <i>W</i>	m s ⁻¹	-
Mean subcloudy layer <i>W</i>	m s ⁻¹	-
Cloud buoyancy (divided to temperature, humidity, and drag force buoyancy terms)	m s ⁻²	^(a,b)
Mean diffusion (condensation + evaporation) rates	g s ⁻¹	^(a,b)
Mean condensation rates	g s ⁻¹	^(a,b)
Mean evaporation rates	g s ⁻¹	^(a,b)
Mean collection rates	g s ⁻¹	^(a,b)
Mean breakup rates	g s ⁻¹	^(a,b)
Mean of drop size distribution	mm	^(a,b)
Variance of drop size distribution	mm	^(a,b)
Rayleigh reflectivity	mm ⁶ m ⁻³	^(a,b)
Mean effective terminal velocity (<i>η</i>)	m s ⁻¹	-
Variance of <i>η</i>	m s ⁻¹	-
Mean absolute vertical velocity (<i>V</i> _{abs} = <i>W</i> + <i>η</i>)	m s ⁻¹	-
Mean LCL for cloud's pixels	m	-
Mean equilibrium level (EL) for cloud's pixels	m	-
Mean LCL for domain noncloudy pixels	m	-
Mean EL for domain noncloudy pixels	m	-
Cartesian coordinates of cloud total (cloud + rain) COG	-	-

^aVariables divided to cloud core, cloud margin, and cloud total regions separately.

^bVariables that include cloud mean vertical profiles.

Thus, a general form of equation (C1) is

$$\text{LWP} \left[\frac{\text{g}}{\text{m}^2} \right] = \int_0^H \rho \gamma \left(\frac{z}{\zeta} \right)^\beta dz = \frac{\rho \gamma}{(\beta + 1) \zeta^\beta} H^{\beta+1} \quad (\text{C2})$$

where β is a measure for the degree of adiabaticity and can range between 0 (constant LWC profile) and 1 (adiabatic-linear LWC increase with height). For simplicity, we have also assumed constant air density (ρ) with height. This approximation degrades for deep clouds. Using the definition of COG along the vertical axis from equation (1), we get for a cloud column

$$\text{COG} [\text{m}] = \frac{\int_0^H \text{LWC} z dz}{\int_0^H \text{LWC} dz} = \frac{\frac{\rho \gamma}{(\beta+2) \zeta^\beta} H^{\beta+2}}{\text{LWP}}. \quad (\text{C3})$$

Combining equations (C2) and (C3), we obtain a general expression for COG dependence on LWP:

$$\text{COG} [\text{m}] = \frac{(\beta + 1)^{\frac{\beta+2}{\beta+1}}}{\beta + 2} (\rho \gamma)^{-\frac{1}{\beta+1}} \zeta^{\frac{\beta}{\beta+1}} \text{LWP}^{\frac{1}{\beta+1}} \quad (\text{C4})$$

or

$$\begin{aligned} \text{COG} &= a \text{LWP}^b \\ a &= \frac{(\beta+1)^{\beta+1}}{\beta+2} (\rho\gamma)^{-\frac{1}{\beta+1}} \frac{\beta}{\zeta^{\beta+1}}, \\ b &= \frac{1}{\beta+1} \end{aligned} \quad (\text{C5})$$

where a depends strongly on the degree of adiabaticity (β) and weakly on thermodynamic parameters (γ), and b is an equivalent measure for degree of adiabaticity, ranging from 0.5 for the theoretical adiabatic case to 1 for the extreme, constant LWC profile case. Taking a value of $\rho = 1$ and typical γ , ζ , and β values from above, we find a maximum theoretical range of $10 < a < 500$. However, the lowest value for β seen in our simulations was 0.5. Taking this value as our lower bound, the range reduces to $10 < a < 70$.

By applying a power law fit to COG versus LWP data, one can obtain both a and b coefficients. They can then be used to solve for the domain thermodynamic constant (γ):

$$\gamma = \left(\frac{\zeta^{1-b}}{a(\frac{1}{b}+1)b^{1+b}\rho^b} \right)^{\frac{1}{b}} \quad (\text{C6})$$

while also taking $\zeta = 1 \times 10^{-3}$ and $\rho = 1$.

Acknowledgments

The research leading to these results has received funding from the European Research Council under the European Union's Seventh Framework Programme (FP7/2007-2013)/ERC grant agreement 306965. M.O.'s and G.F.'s contributions are supported in part by the U.S. Department of Energy, Office of Science, Biological and Environmental Research under the Atmospheric System Research (ASR) Program. Pacific Northwest National Laboratory is operated by Battelle for the U.S. Department of Energy under contract DE-AC06-76RLO1830. A.B.K. was supported, in part, by NSF AGS-1119164. The authors acknowledge Marat Khairoutdinov for making SAM model available for this study, available at: <http://rossby.msrb.sunysb.edu/~marat/SAM.html>. The SBM microphysics scheme was developed and implemented by A.P.K. and M.O. Simulations setup details are available in the appendix of [Siebesma et al., 2003] for BOMEX case study and 10.3334/ORNLDAAC/1114 for AMAZON case study. We thank the HPC staff in Weizmann computer center for helping with technical modeling issues and the anonymous reviewers for their contribution to this work.

References

- Altartaz, O., I. Koren, T. Reislin, A. B. Kostinski, G. Feingold, Z. Levin, and Y. Yin (2008), Aerosols' influence on the interplay between condensation, evaporation and rain in warm cumulus cloud, *Atmos. Chem. Phys.*, 8(1), 15–24, doi:10.5194/acp-8-15-2008.
- Baker, M. B., and T. Peter (2008), Small-scale cloud processes and climate, *Nature*, 451(7176), 299–300, doi:10.1038/nature06594.
- Benner, T. C., and J. A. Curry (1998), Characteristics of small tropical cumulus clouds and their impact on the environment, *J. Geophys. Res.*, 103(D22), 28,753–28,767, doi:10.1029/98JD02579.
- Blyth, A. M. (1993), Entrainment in cumulus clouds, *J. Appl. Meteorol.*, 32(4), 626–641, doi:10.1175/1520-0450(1993)032<0626:eicc>2.0.co;2.
- Blyth, A. M., W. A. Cooper, and J. B. Jensen (1988), A study of the source of entrained air in Montana cumuli, *J. Atmos. Sci.*, 45(24), 3944–3964, doi:10.1175/1520-0469(1988)045<3944:ASOTSO>2.0.CO;2.
- Bony, S., and J.-L. Dufresne (2005), Marine boundary layer clouds at the heart of tropical cloud feedback uncertainties in climate models, *Geophys. Res. Lett.*, 32, L20806, doi:10.1029/2005GL023851.
- Cohen, B. G., and G. C. Craig (2006), Fluctuations in an equilibrium convective ensemble. Part II: Numerical experiments, *J. Atmos. Sci.*, 63(8), 2005–2015, doi:10.1175/JAS3710.1.
- Cotton, W. R., G. Bryan, and S. C. van den Heever (2011), Chapter 7—Cumulus clouds, in *International Geophysics*, edited by G. B. William Cotton and H. van den Susan, pp. 243–314, Academic Press, doi:10.1016/S0074-6142(10)09913-4.
- Dagan, G., I. Koren, and O. Altartaz (2015), Competition between core and periphery-based processes in warm convective clouds—From invigoration to suppression, *Atmos. Chem. Phys.*, 15(5), 2749–2760, doi:10.5194/acp-15-2749-2015.
- Dawe, J. T., and P. H. Austin (2012), Statistical analysis of an LES shallow cumulus cloud ensemble using a cloud tracking algorithm, *Atmos. Chem. Phys.*, 12(2), 1101–1119, doi:10.5194/acp-12-1101-2012.
- de Roode, S. R., and C. S. Bretherton (2003), Mass-flux budgets of shallow cumulus clouds, *J. Atmos. Sci.*, 60(1), 137–151, doi:10.1175/1520-0469(2003)060<0137:MFBOSC>2.0.CO;2.
- Dias, M. A., P. L. S. Dias, M. Longo, D. R. Fitzjarrald, and A. S. Denning (2012), *LBA-ECO CD-01 Meteorological Data, Tapajos and Amazon Rivers, Santarem, Brazil: 2001, Data Set*, Oak Ridge National Laboratory Distributed Active Archive Center, Oak Ridge, Tenn., doi:10.3334/ORNLDAAC/1114.
- Fan, J., M. Ovchinnikov, J. M. Comstock, S. A. McFarlane, and A. P. Khain (2009), Ice formation in Arctic mixed-phase clouds: Insights from a 3-D cloud-resolving model with size-resolved aerosol and cloud microphysics, *J. Geophys. Res.*, 114, D04205, doi:10.1029/2008JD010782.
- Garstang, M., and A. K. Betts (1974), A review of the tropical boundary layer and cumulus convection: Structure, parameterization, and modeling, *Bull. Am. Meteorol. Soc.*, 55(10), 1195–1205.
- Grabowski, W. W., et al. (2006), Daytime convective development over land: A model intercomparison based on LBA observations, *Q. J. R. Meteorol. Soc.*, 132(615), 317–344, doi:10.1256/qj.04.147.
- Grant, A. L. M., and A. P. Lock (2004), The turbulent kinetic energy budget for shallow cumulus convection, *Q. J. R. Meteorol. Soc.*, 130(597), 401–422, doi:10.1256/qj.03.50.
- Handwerker, J. (2002), Cell tracking with TRACE3D—A new algorithm, *Atmos. Res.*, 61(1), 15–34, doi:10.1016/S0169-8095(01)00100-4.
- Heiblum, R. H., et al. (2016), Characterization of cumulus cloud fields using trajectories in the center of gravity versus water mass phase space: 2. Aerosol effects on warm convective clouds, *J. Geophys. Res. Atmos.*, 121, doi:10.1002/2015JD024193.
- Heus, T., and A. Seifert (2013), Automated tracking of shallow cumulus clouds in large domain, long duration large eddy simulations, *Geosci. Model Dev.*, 6(4), 1261–1273, doi:10.5194/gmd-6-1261-2013.
- Heus, T., H. J. J. Jonker, H. E. A. Van den Akker, E. J. Griffith, M. Koutek, and F. H. Post (2009), A statistical approach to the life cycle analysis of cumulus clouds selected in a virtual reality environment, *J. Geophys. Res.*, 114, D06208, doi:10.1029/2008JD010917.
- Holland, J. Z., and E. M. Rasmusson (1973), Measurements of the atmospheric mass, energy, and momentum budgets over a 500-kilometer square of tropical ocean, *Mon. Weather Rev.*, 101(1), 44–55, doi:10.1175/1520-0493(1973)101<0044:MOTAME>2.3.CO;2.
- Jaenicke, R. (1988), 9.3.1 Physical properties, in *Physical and Chemical Properties of the Air*, edited by G. Fischer, pp. 405–420, Springer, Berlin, doi:10.1007/10333390_72.
- Jiang, H., H. W. Xue, A. Teller, G. Feingold, and Z. Levin (2006), Aerosol effects on the lifetime of shallow cumulus, *Geophys. Res. Lett.*, 33, L14806, doi:10.1029/2006GL026024.

- Jiang, H., G. Feingold, H. H. Jonsson, M.-L. Lu, P. Y. Chuang, R. C. Flagan, and J. H. Seinfeld (2008), Statistical comparison of properties of simulated and observed cumulus clouds in the vicinity of Houston during the Gulf of Mexico Atmospheric Composition and Climate Study (GoMACCS), *J. Geophys. Res.*, *113*, D13205, doi:10.1029/2007JD009304.
- Khain, A. P. (2009), Notes on state-of-the-art investigations of aerosol effects on precipitation: A critical review, *Environ. Res. Lett.*, *4*(1), 015004 (015020 pp.), doi:10.1088/1748-9326/4/1/015004.
- Khain, A. P., M. Ovchinnikov, M. Pinsky, A. Pokrovsky, and H. Krugliak (2000), Notes on the state-of-the-art numerical modeling of cloud microphysics, *Atmos. Res.*, *55*(3–4), 159–224, doi:10.1016/S0169-8095(00)00064-8.
- Khain, A. P., A. Pokrovsky, M. Pinsky, A. Seifert, and V. Phillips (2004), Simulation of effects of atmospheric aerosols on deep turbulent convective clouds using a spectral microphysics mixed-phase cumulus cloud model. Part I: Model description and possible applications, *J. Atmos. Sci.*, *61*(24), 2963–2982, doi:10.1175/JAS-3350.1.
- Khain, A. P., T. V. Prabha, N. Benmoshe, G. Pandithurai, and M. Ovchinnikov (2013), The mechanism of first raindrops formation in deep convective clouds, *J. Geophys. Res. Atmos.*, *118*, 9123–9140, doi:10.1002/jgrd.50641.
- Khairoutdinov, M. F., and D. A. Randall (2003), Cloud resolving modeling of the ARM summer 1997 IOP: Model formulation, results, uncertainties, and sensitivities, *J. Atmos. Sci.*, *60*(4), 607–625, doi:10.1175/1520-0469(2003)060<0607:CRMOTA>2.0.CO;2.
- Koren, I., O. Altaratz, G. Feingold, Z. Levin, and T. Reislin (2009), Cloud's center of gravity—A compact approach to analyze convective cloud development, *Atmos. Chem. Phys.*, *9*(1), 155–161, doi:10.5194/acp-9-155-2009.
- Kostinski, A. B. (2008), Drizzle rates versus cloud depths for marine stratocumuli, *Environ. Res. Lett.*, *3*(4), 045019, doi:10.1088/1748-9326/3/4/045019.
- Lu, C., Y. Liu, G. J. Zhang, X. Wu, S. Endo, L. Cao, Y. Li, and X. Guo (2015), Improving parameterization of entrainment rate for shallow convection with aircraft measurements and large eddy simulation, *J. Atmos. Sci.*, doi:10.1175/JAS-D-15-0050.1.
- Malkus, J. S. (1958), On the structure of the trade wind moist layer, *Pap. Phys. Oceanogr. Meteorol.*, doi:10.1575/1912/5443.
- Meerkötter, R., and L. Bugliaro (2009), Diurnal evolution of cloud base heights in convective cloud fields from MSG/SEVIRI data, *Atmos. Chem. Phys.*, *9*(5), 1767–1778, doi:10.5194/acp-9-1767-2009.
- Neggers, R. A. J., B. Stevens, and J. D. Neelin (2007), Variance scaling in shallow-cumulus-topped mixed layers, *Q. J. R. Meteorol. Soc.*, *133*(628), 1629–1641, doi:10.1002/qj.105.
- Nuijens, L., I. Serikov, L. Hirsch, K. Lonitz, and B. Stevens (2013), The distribution and variability of low-level cloud in the North-Atlantic trades, *Q. J. R. Meteorol. Soc.*, doi:10.1002/qj.2307.
- Plant, R. S. (2009), Statistical properties of cloud lifecycles in cloud-resolving models, *Atmos. Chem. Phys.*, *9*(6), 2195–2205, doi:10.5194/acp-9-2195-2009.
- Pontikis, C. A. (1996), Parameterization of the droplet effective radius of warm layer clouds, *Geophys. Res. Lett.*, *23*(19), 2629–2632, doi:10.1029/96GL02452.
- Rauber, R. M., H. T. Ochs III, L. Di Girolamo, S. Göke, E. Snodgrass, B. Stevens, C. Knight, J. B. Jensen, D. H. Lenschow, and R. A. Rilling (2007), Rain in shallow cumulus over the ocean: The RICO campaign, *Bull. Am. Meteorol. Soc.*, *88*(12), 1912–1928, doi:10.1175/BAMS-88-12-1912.
- Short, D. A., and K. Nakamura (2000), TRMM radar observations of shallow precipitation over the tropical oceans, *J. Clim.*, *13*(23), 4107–4124, doi:10.1175/1520-0442(2000)013<4107:TROOSP>2.0.CO;2.
- Siebesma, A. P., C. S. Bretherton, A. Brown, A. Chlond, J. Cuxart, P. G. Duynkerke, H. Jiang, M. F. Khairoutdinov, D. Lewellen, and C. H. Moeng (2003), A large eddy simulation intercomparison study of shallow cumulus convection, *J. Atmos. Sci.*, *60*(10), 1201–1219, doi:10.1175/1520-0469(2003)060<1201:ALESIS>2.0.CO;2.
- Squires, P. (1958), Penetrative downdraughts in cumuli, *Tellus*, *10*(3), 381–389, doi:10.1111/j.2153-3490.1958.tb02025.x.
- Stevens, B., and G. Feingold (2009), Untangling aerosol effects on clouds and precipitation in a buffered system, *Nature*, *461*(7264), 607–613, doi:10.1038/nature08281.
- Tao, W.-K., J.-P. Chen, Z. Li, C. Wang, and C. Zhang (2012), Impact of aerosols on convective clouds and precipitation, *Rev. Geophys.*, *50*, RG2001, doi:10.1029/2011RG000369.
- Trenberth, K. E., J. T. Fasullo, and J. Kiehl (2009), Earth's global energy budget, *Bull. Am. Meteorol. Soc.*, *90*(3), 311–323, doi:10.1175/2008BAMS2634.1.
- Warner, J. (1955), The water content of cumuliform cloud, *Tellus*, *7*(4), 449–457, doi:10.1111/j.2153-3490.1955.tb01183.x.
- Warren, S. G., C. J. Hahn, J. London, R. M. Chervin, and R. L. Jenne (1986), Global distribution of total cloud cover and cloud type amounts over land, Rep. Washington Univ., Seattle (USA). Dept. of Atmospheric Sciences; Colorado Univ., Boulder (USA); Natl. Center for Atmos. Res., Boulder, Colo.
- Warren, S. G., C. J. Hahn, and J. London (1988), Global distribution of total cloud cover and cloud type amounts over the ocean, Rep. USDOE Office of Energy Research, Washington, DC (USA). Carbon Dioxide Research Div.; Natl. Center for Atmos. Res., Boulder, Colo.
- Wielicki, B. A., T. Wong, N. Loeb, P. Minnis, K. Priestley, and R. Kandel (2005), Changes in Earth's albedo measured by satellite, *Science*, *308*(5723), 825, doi:10.1126/science.1106484.
- Witte, M. K., P. Y. Chuang, and G. Feingold (2014), On clocks and clouds, *Atmos. Chem. Phys.*, *14*(13), 6729–6738, doi:10.5194/acp-14-6729-2014.
- Xue, H. W., and G. Feingold (2006), Large-eddy simulations of trade wind cumuli: Investigation of aerosol indirect effects, *J. Atmos. Sci.*, *63*(6), 1605–1622, doi:10.1175/jas3706.1.
- Zhao, G., and L. Di Girolamo (2007), Statistics on the macrophysical properties of trade wind cumuli over the tropical western Atlantic, *J. Geophys. Res.*, *112*, D10204, doi:10.1029/2006JD007371.
- Zhao, M., and P. H. Austin (2005), Life cycle of numerically simulated shallow cumulus clouds. Part I: Transport, *J. Atmos. Sci.*, *62*(5), 1269–1290, doi:10.1175/jas3414.1.